

Highlights

Semi-analytical solution for sound propagation from a moving directional source in a shallow-water waveguide

Tengjiao He, Xinyu Liu, Ruixin Nie, Wei Guo, Shiqi Mo, Bin Wang

- A semi-analytical solution for sound propagation from a directional source moving in shallow water is presented.
- The presented semi-analytical solution is valid for any range independent environment with an arbitrary sound-speed profile.
- A novel normal-mode model is developed, which comprehensively accounts for the Doppler-induced impact.
- The Doppler beam shift is found and investigated using the proposed theory.
- The observed angular offset of modal plane waves can be attributed to the Doppler beam shift.

Tengjiao He^{a,1}, Xinyu Liu^b, Ruixin Nie^{a,1}, Wei Guo^c, Shiqi Mo^d and Bin Wang^{a,*,1}

^aKey Laboratory of Marine Intelligent Equipment and System, Ministry of Education, Shanghai Jiao Tong University, Shanghai, 200240, P. R. China

^bChina Ship Scientific Research Center, Wuxi, 214000, P. R. China

^cCollege of Meteorology and Oceanography, National University of Defense Technology, Changsha, 410073, P. R. China

^dCollege of Underwater Acoustic Engineering, Harbin Engineering University, Harbin, 150001, P. R. China

ARTICLE INFO

Keywords:

moving directional sources
semi-analytical method
Doppler-shifted field
normal-mode model
Doppler beam shift

ABSTRACT

Understanding the waveguide fields produced by moving directional sources is of crucial importance in underwater acoustic detection. In practice, moving underwater targets often exhibit directionality, especially at high frequencies. Herein, we present a semi-analytical method to calculate the Doppler-shifted field (DSF) from a directional source moving horizontally in a range-independent, shallow-water waveguide. We develop a novel normal-mode model using a modal-projection approach with a perfectly matched layer. This comprehensively accounts for changes in modal shape, eigenvalue shifts, and the branch-integral contribution. We derive an analytical expression for the DSF based on Huygens' principle, and the solution is presented as a sum over propagating eigenmodes, with the modal excitation determined by the source directivity depending upon the grazing angle of each pair of modal plane waves. This rigorous expression is valid for any type of radiator moving in a range-independent environment with an arbitrary sound-speed profile. We then present a theoretical analysis of the Doppler beam shift produced by a piston-like radiator. This reveals that the observed angular offset of modal plane waves can be attributed to the Doppler beam shift and confirms that this is a new mechanism causing considerable differences between the fields generated by a directional moving source and by the same source at rest. This has potential value in various applications, particularly for underwater acoustic detection of moving targets.

1. Introduction

Driven by acoustic fault diagnosis (Shen et al., 2016) and sound-source localization and identification (Zhang et al., 2016), there has been considerable interest in the characteristics of the sound fields created by moving sources such as land vehicles, trains (Barsikow and King, 1988), and aircraft (Stoker et al., 2003). Doppler effects, which are induced by the relative motion between a source and a receiver, have been investigated thoroughly in an infinite homogeneous medium (Lowson, 1965; Pierce and Beyer, 1990; Makarewicz, 1992) and also in relation to underwater acoustics, because this is vital for assessing sonar performance and inversion of ocean-environment parameters (Jensen et al., 2011). Doppler phenomena in underwater environments, in which reflection, refraction, and scattering occur (He et al., 2021, 2023b), are complicated. Flanagan et al. (1974) and Clark et al. (1976) carried out pioneering work in deep ocean channels, initially investigating Doppler-spreading effects by analyzing the multi-path signal emitted by a distant moving source. Furthermore, in the deep ocean environment, Dzieciuch and Munk (1994) classified ray arrivals using experimentally observed differential Doppler shifts.

In recent years, there has been an increasing focus on shallow-water Doppler phenomena. Numerous well-established theories, such as ray tracing (Guthrie et al., 1974), normal modes (NMs) (Neubert, 1977; Hawker, 1979; Buckingham and Giddens, 2006), and wavenumber integration (Schmidt and Kuperman, 1994) have been employed for investigating these phenomena. Helped by their analytical form being connected to waveguide physics, NMs have been used widely to shed light on waveguide Doppler behavior. Obrezanova and Rabinovich (1998) derived asymptotic formulas for the Doppler-shifted field (DSF) generated by a moving source in a two-layer waveguide, giving a clear physical interpretation of Doppler effects in terms of retarded times. Rabinovich and Hernández Juárez (2016) developed a spectral-parameter power-series method that provides a numerically efficient solution for the

*Corresponding author

 bin_wang@sjtu.edu.cn (B. Wang)

ORCID(s):

¹Also at: Department of Naval Architecture and Ocean Engineering, Shanghai Jiao Tong University, Shanghai, 200240, P. R. China

high-frequency underwater DSF due to a moving source submerged in the ocean. Additionally, the DSFs produced by aerial targets have attracted significant interest; this is because detecting aircraft-generated noise with submerged hydrophones enables estimation of the sound speed in water and sediment, as well as providing means to obtain the motion parameters of airborne sources (Buckingham et al., 2002; Amiri-Simkooei et al., 2008; Lo and Ferguson, 2013; Bevans and Buckingham, 2017; Haijie et al., 2019). Buckingham and Giddens (2006) developed a theoretical model of the DSF generated by an aircraft in an air–ocean–sediment waveguide; based on NMs, they derived an analytical solution for the three-layer DSF, using an NM-based model to study shallow-water Doppler effects and using ray theory to interpret the mechanism of Doppler spreading in a straightforward manner. Nevertheless, conventional NM-based approaches have drawbacks, as they often ignore changes in modal shapes and the contribution of the branch integral, leading to inaccurate description of the Doppler-induced modal cut-off.

Acoustic radiation emitted from underwater sources is typically directional. Incorporating the directional characteristics of a source into simulations of waveguide DSFs has received significant interest because source directivity is a crucial consideration for various applications, including underwater acoustic detection. However, integrating source directivity into waveguide-field simulations has been a longstanding challenge.

Monopole point sources and multipoles are the two types of basis function that are used to represent source directivity. The former relies on Huygens' principle, expressing the directional radiation as a field superposition from an array of monopole point sources. The amplitudes and phases of these point sources are determined by matching the radiated field or the normal particle velocities distributed over the surface of the source. This method is typically used to predict sound propagation from vibrating elastic structures in shallow water (He et al., 2023a; Fu et al., 2020; Petris et al., 2022; Jiang et al., 2020). In contrast, multipole representations employ spherical harmonic functions to expand the source directivity, allowing the waveguide field resulting from a directional source to be considered as a superposition of a complete and orthogonal basis set. An example in this context is an outdoor sound-propagation model that incorporates parabolic-equation algorithms with spherical harmonic expansion Vecherin et al. (2011, 2012). In room acoustics, a recent paper also reported using a similar approach to predict the reverberation field produced by a directional radiator within a cavity (Zhong et al., 2023). While both numerical approaches are able to incorporate source directivity when simulating the waveguide field, they can also have a considerable computational cost for high-frequency problems in which strong source directivity is expected, as these may involve a large number of point sources or high-order basis functions. Moreover, these numerical approaches do not provide direct insights into the underlying waveguide physics.

In light of the above discussion, the objectives of this work are twofold: first, to develop an improved NM model capable of handling changing modal shapes, eigenvalue Doppler shifts, and the contribution of the branch-cut integral; and second, to derive an analytical, NM-based expression for the DSF resulting from a directional source moving in shallow water. This article presents a novel semi-analytical method for calculating the DSF resulting from a directional source in shallow water with an arbitrary sound-speed profile (SSP). The proposed method offers faster solutions than fully numerical techniques while also providing more precise descriptions of Doppler-induced effects than standard NM-based approaches. Furthermore, this method contributes to a deeper understanding of the waveguide physics involved. Notably, no semi-analytical solutions have been developed for this specific problem, highlighting the originality of this article's contribution.

To analyze the field generated by a moving source, we transform it into the field generated by the same source at rest in a homogeneous moving medium (Ostashev and Wilson, 2015). The ocean environment is represented as a classic shallow-water waveguide underneath a free surface. To accurately describe the Doppler-affected waveguide physics, we use a modal-projection method with a perfectly matched layer (PML) (He et al., 2021) to yield and close the associated generalized matrix eigenproblem, which can be easily solved using matrix eigenvalue decomposition. This approach enables solving of the exact wave equation for sound propagation in an open waveguide with uniform flow, in which the branch-cut integral is replaced by a sum over high-order modes. After this, we derive an analytical, normal-mode expression for the DSF due to a directional source moving in a two-layer waveguide. Based on Huygens' principle, the DSF due to the moving directional source is replaced with a field superposition from an array of point sources placed over the surface of the source. Instead of evaluating the integral of this field superposition numerically, we derive an analytical expression for the integral by introducing the Fraunhofer far-field approximation and a Taylor-series expansion to the integral kernel. This derivation eventually yields the modal expression for the DSF as a summation over propagating eigenmodes, with their modal excitations determined by the source directivity depending on the grazing angle of each pair of modal plane waves. The derived modal expression is rigorous, and it is thus valid for sources with arbitrary directivities in a range-independent waveguide with an arbitrary SSP.

The proposed theoretical model is used to investigate the Doppler beam shift generated by a piston-like radiator in a two-layer waveguide. The interpretations provided by this theoretical model reveal the underlying mechanism involved. Moreover, the analysis demonstrates that the Doppler beam shift acts as a third mechanism in addition to changing modal shapes and eigenvalues shifts, leading to significant differences that can be used to distinguish the fields generated by a moving directional source and by the same source at rest.

The remainder of this paper is organized as follows. Section 2 presents the equations for the two-layer DSF due to a moving directional source, including the exact governing wave equations and a general derivation of the modal expression for the DSF. Section 3 presents numerical simulations, including validation cases and analyses of the Doppler beam shift induced by a piston-like radiator moving in shallow water. Finally, conclusions are drawn in Section. 4.

2. Normal-mode solution for Doppler-shifted field in an ocean–sediment waveguide

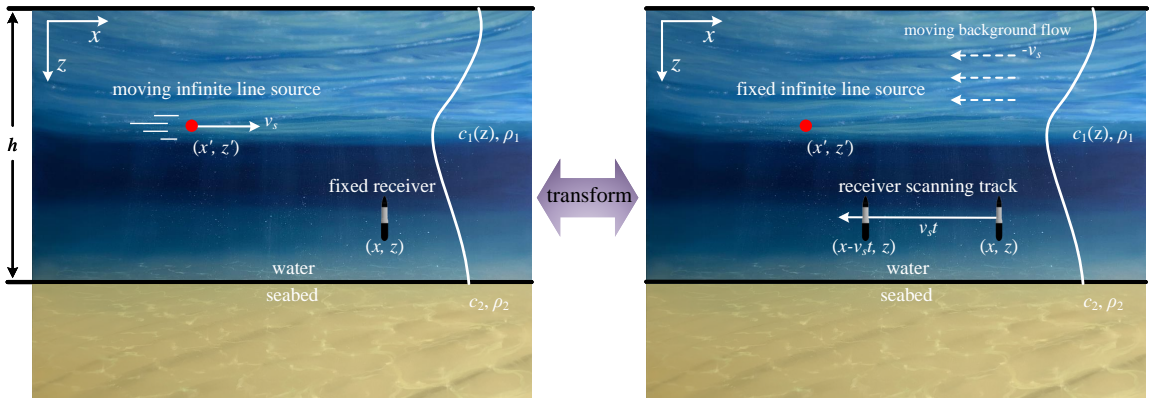


Figure 1: Schematic of two-layer waveguide considered in present analysis, where the underwater domain is represented by a soft-wall waveguide (with two Dirichlet boundaries). The infinite line source in the transverse direction moves horizontally at a fixed depth $z = z'$ with a constant moving velocity of v_s . The sound speed of the water is depth-dependent. The first plot shows the original coordinate system with a moving source and a fixed receiver. The second plot displays the transformed coordinate system, in which the sound field received by the fixed hydrophone at t is converted into a spatial scan using a horizontal hydrophone array. The spatial scan spans from (x, z) to $(x - v_s t, z)$, assuming that the source is stationary in a homogeneous moving medium with a flow velocity of $-v_s$.

The following analysis considers the two-layer waveguide shown in Fig. 1, with layers 1, and 2 representing the ocean and sediment, respectively. Here, ρ_j and c_j with $j = 1, 2$ represent the density and sound speed, respectively, of each layer. For simplicity, the problem is reduced to a 2D range-independent waveguide. For the problem, x and z are the range and depth coordinates, respectively, and we consider an infinite line source at a fixed depth $z = z'$ below the sea surface. The line source moves horizontally with a constant velocity of v_s . The following analysis presents the novel NM model that fully accounts for the Doppler-affected modal shapes and eigenvalues. It begins by describing the exact governing wave equations and subsequently introduces the modal projection method along with the modal solution for an omni-directional point-source. The subsequent part of this section focuses on deriving the modal expression for the DSF resulting from a directional radiator moving in a two-layer waveguide.

2.1. A novel normal-mode model for calculating the Doppler-shifted field due to a point source moving in shallow water

Calculating the DSF due to a submerged moving source typically starts with the Helmholtz equation for a motionless fluid but with a varying source position. Herein, the linearized fluid dynamics equations for a homogeneous moving medium are recalled to calculate the flow-affected sound field. The DSF generated by a moving source in a motionless medium then reduces to that excited by the same source at rest in an equivalent homogeneous moving medium (Ostashev and Wilson, 2015). Therefore, the DSF due to the source moving to $(x' + v_s t, z')$ at time t , with a receiver fixed at (x, z) , is converted to a spatial scan using a horizontal hydrophone array. The spatial scan spans from (x, z) to $(x - v_s t, z)$, assuming that the source is stationary at (x', z') in a homogeneous moving medium with

a flow velocity of $-v_s$. Fig. 1 illustrates this transformation from the original coordinate system, where the source is moving, to the transformed coordinate system, where the source is at rest in a homogeneous moving medium. It is important to note that in the transformed coordinate system, the spatial scan by the horizontal array does not introduce any additional motion-induced effects; it simply changes the receiver position. The Doppler effect can be considered by accounting for the motion of the medium.

2.1.1. Governing equations

The analysis assumes that the ocean is stratified, which means that the sound speed depends on z only. The medium moves with a positive flow velocity of v_s in the negative x direction to account for the source motion. There is a motionless receiver at (x, z) , and at time $t = 0$ there is a submerged source at (x', z') moving with a constant velocity of v_s in the positive x direction. Using the linearized fluid dynamics equations, the governing equations for the current analysis are (Nijs and Wapenaar, 1990)

$$\begin{cases} \nabla \cdot \mathbf{u} + \frac{1}{K} \left(\frac{\partial}{\partial t} + \mathbf{v} \cdot \nabla \right) p = 0, \\ \nabla p + \rho \left(\frac{\partial}{\partial t} + \mathbf{v} \cdot \nabla \right) \mathbf{u} + \rho u_z \frac{\partial \mathbf{v}}{\partial z} = 0, \end{cases} \quad (1)$$

where p and $\mathbf{u} = [u_x, u_z]^T$ are the acoustic pressure and particle velocity in the water, respectively, $\mathbf{v} = [-v_s, 0]^T$ is the total flow velocity that accounts for the source motion, and K is the compression modulus. Here, the superscript T denotes the transpose.

Applying the time–frequency Fourier transform to both the pressure and particle velocity gives the frequency-domain wave equations, and introducing a new variable $\mu = 1 + v_s k_r / \omega$ yields

$$\begin{aligned} \frac{\partial U_z}{\partial z} - i k_r U_x + \frac{i \omega}{K} \mu P &= 0, \\ -i k_r P + i \omega \rho \mu U_x &= 0, \\ \frac{\partial P}{\partial z} + i \omega \rho \mu U_z &= 0, \end{aligned} \quad (2)$$

where $P(k_r, z, \omega)$, $U_x(k_r, z, \omega)$, and $U_z(k_r, z, \omega)$ are the Fourier transforms of $p(x, z, t)$, $u_x(x, z, t)$, and $u_z(x, z, t)$, respectively, with k_r denoting the horizontal wavenumber in the water, and ω is the angular frequency. The depth-dependent wave equation for P is then obtained by eliminating U from the first equation in Eq. (2):

$$\frac{\partial^2 P}{\partial z^2} + (\mu^2 k^2 - k_r^2) P = 0, \quad (3)$$

where $k = \sqrt{\omega^2 \rho / K}$ is the wavenumber, with the solution subject to the boundary conditions at the air–water and water–sediment interfaces:

$$\begin{aligned} P|_{z=0} &= 0, \\ P|_{z=-h^+} &= P|_{z=-h^-}, \\ \frac{1}{\rho_1} \frac{\partial P}{\partial z} \Big|_{z=-h^+} &= \frac{1}{\rho_2} \frac{\partial P}{\partial z} \Big|_{z=-h^-}, \end{aligned} \quad (4)$$

2.1.2. Modal projection method incorporating perfectly matched layers

Based on modal theory, the solution of the 2D wave equation can be written as

$$p(x, z, t) = \sum_{n=1}^{\infty} A_{(n)} P_{(n)}(z) \frac{e^{-i k_{r(n)}(x-x'-v_s t)}}{k_{r(n)}}, \quad (5)$$

where $P_{(n)}$ are the eigenfunctions, $A_{(n)}$ are the modal amplitudes, $k_{r(n)}$ are the corresponding eigenvalues, and the subscript n denotes the order of the eigenfunction. Note that $P_{(n)}$ are the solutions of Eq. (3) subject to the boundary condition in Eq. (4). A modal-domain eigenequation can be obtained by substituting $P_{(n)}$ back into Eq. (3), and after some rearranging, this yields

$$[G_0 + G_1 k_{r(n)} + G_2 k_{r(n)}^2] P_{(n)}(z) = 0, \quad (6)$$

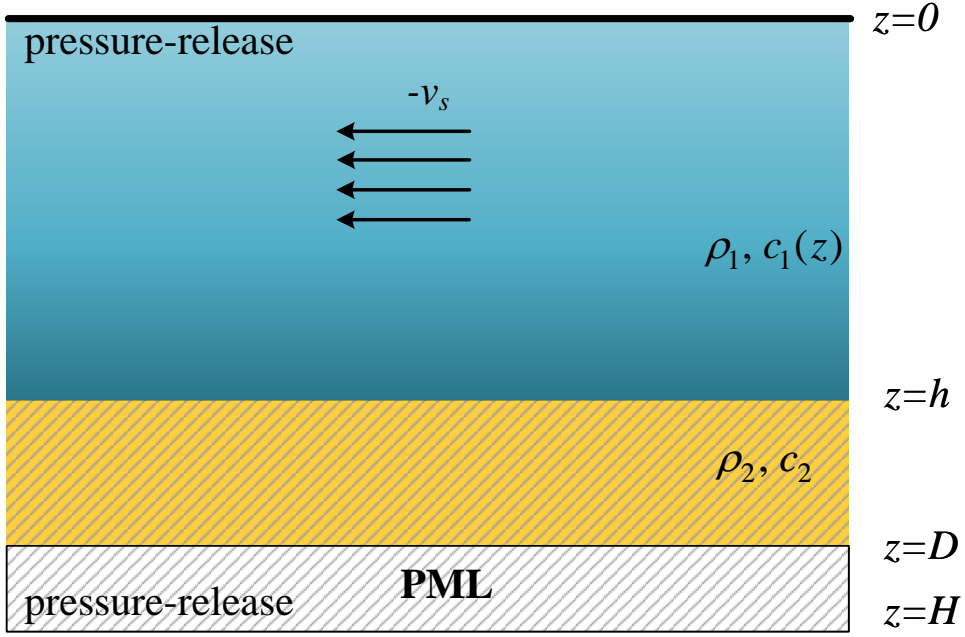


Figure 2: Schematic of the underwater domain that is represented by a soft-wall waveguide (with two Dirichlet boundaries). Perfectly matched layer is used to truncate the underwater domain to absorb outgoing waves.

where

$$\begin{aligned} G_0 &= \frac{\partial^2}{\partial \hat{z}^2} + k_j^2, \\ G_1 &= 2k_j M_j, \\ G_2 &= M_j^2 - 1, \end{aligned} \quad (7)$$

where $M_j = v_s/c_j$ is the Mach number in the water ($j = 1$) or sediment ($j = 2$). Equation (6)—the square eigenequation in $k_{r(n)}$ —is then solved using a modal projection method.

In the current analysis, the underwater domain shown in Fig. 2 is treated as a half-space (open waveguide) below a Dirichlet boundary. A PML is used to truncate the half-space and absorb the outgoing waves at $z = \infty$, thereby closing the eigenequation associated with the open waveguide. Two Dirichlet boundary conditions are imposed at $z = 0$ and $z = H$ for the bounded space, with the PML extending from $z = D$ to $z = H$. The PML is mathematically equivalent to stretching the complex coordinates (Berenger, 1994), i.e.,

$$\hat{z} = z + i \int_0^z \sigma(\epsilon) d\epsilon, \quad (8)$$

where $\sigma(\epsilon)$ is the damping function and $\epsilon = (z - D)/(H - D)$ is the dimensionless coordinate. Here, a second-degree polynomial damping function is used, expressed mathematically as $\sigma(\epsilon) = \zeta \epsilon^2$ (Singer and Turkel, 2004; Rabinovich et al., 2010), where ζ is a positive real damping coefficient controlling the rate of damping. From Eq. (8), we obtain

$$\begin{aligned} \frac{\partial}{\partial \hat{z}} &= \frac{1}{s(z)} \frac{\partial}{\partial z}, \\ d\hat{z} &= s(z) dz, \end{aligned} \quad (9)$$

where

$$\begin{aligned} s(z) &= 1, \quad 0 < z < D, \\ s(z) &= 1 + i\sigma(z), \quad D < z < H. \end{aligned} \quad (10)$$

Next, $P_{(n)}$ are projected onto a series of basis functions selected by satisfying the two boundary conditions at $z = 0$ and $z = H$:

$$\begin{cases} P_{(n)}(z) = \sum_{m=1}^N w_{(m,n)} \phi_{(m)}(z) = \mathbf{\Phi} \mathbf{w}, \\ \phi_{(m)}(z) = \sqrt{\frac{2}{H}} \sin \left[\frac{m\pi}{H} z \right]. \end{cases} \quad (11)$$

where $\phi_{(m)}$ are the basis modes for the bounded space in the ocean, $w_{(m,n)}$ are the projection coefficients, $\mathbf{\Phi}$ and \mathbf{w} represent $1 \times N$ row vectors of the basis modes and projection coefficients, respectively, and N and the subscript m are the total number and order of the basis modes, respectively. Weighting Eq. (6) by $\frac{1}{\rho_j} \mathbf{\Phi}^T$ and integrating the weighted eigenequation over $0 \leq z \leq H$ yields

$$\int_0^H \frac{1}{\rho_j} \mathbf{\Phi}^T [G_0 + G_1 k_{r(n)} + G_2 k_{r(n)}^2] P_{(n)}(z) dz = 0. \quad (12)$$

Next, we consider the projection of $P_{(n)}$ onto the space spanned by $\phi_{(m)}$ and perform integration by parts to reduce the second-order derivatives to first-order ones. Requiring $P_{(n)}$ to be continuous across the water–sediment interface, we obtain the matrix equation

$$[\mathbf{\Gamma} + k_r \mathbf{\Pi} + k_r^2 \mathbf{\Upsilon}] \mathbf{W} = 0, \quad (13)$$

where \mathbf{W} is an $N \times N$ projection-coefficient matrix, and $\mathbf{\Gamma}$, $\mathbf{\Pi}$, and $\mathbf{\Upsilon}$ are

$$\begin{aligned} \mathbf{\Gamma} &= \int_0^H -\frac{1}{\rho_j} \left[\frac{1}{s(z)} \frac{\partial \mathbf{\Phi}^T}{\partial z} \frac{\partial \mathbf{\Phi}}{\partial z} - k_j^2 s(z) \mathbf{\Phi}^T \mathbf{\Phi} \right] dz, \\ \mathbf{\Pi} &= \int_0^H \frac{1}{\rho_j} 2k_j M_j s(z) \mathbf{\Phi}^T \mathbf{\Phi} dz, \\ \mathbf{\Upsilon} &= \int_0^H \frac{1}{\rho_j} (M_j^2 - 1) s(z) \mathbf{\Phi}^T \mathbf{\Phi} dz. \end{aligned} \quad (14)$$

Note that analytical expressions can be derived for the integrals containing the first-order derivatives in $\mathbf{\Gamma}$ and the first-order term in $\mathbf{\Upsilon}$. However, the remaining parts in the above equations must be integrated numerically. The numerical scheme follows the Clenshaw–Curtis quadrature rules (Waldvogel, 2006; He et al., 2020, 2021), which provide excellent convergence using relatively few depth samplings; generally, five points per period of the basis modes are sufficient to ensure good convergence (He et al., 2021). A generalized matrix eigenvalue problem can be obtained by rearranging Eq. (13) as follows :

$$\begin{bmatrix} \mathbf{\Gamma} & \mathbf{0} \\ \mathbf{0} & \mathbf{\Upsilon}^T \end{bmatrix} \begin{bmatrix} \mathbf{W} \\ k_r \mathbf{W} \end{bmatrix} = k_r \begin{bmatrix} \mathbf{\Pi} & \mathbf{\Upsilon} \\ \mathbf{\Upsilon}^T & \mathbf{0} \end{bmatrix} \begin{bmatrix} \mathbf{W} \\ k_r \mathbf{W} \end{bmatrix}. \quad (15)$$

After solving the above eigenvalue problem, the eigenvalues must be sorted in order, and their eigenvectors represent the projection coefficients. The eigenfunctions $P_{(n)}(z)$ are reconstructed using the projection defined in Eq. (11). It is evident that the generalized matrix eigenvalue problem exhibits the dependency of Mach number, as the sub-matrix block, calculated by Eq. (14), is clearly a function of M_j . Fundamentally, the depth-separated wave equation, as per Eq. (6), yields distinct generalized matrix eigenvalue problems for different Mach numbers. Consequently, this leads to the determination of various eigenvalues and eigenfunctions corresponding to varying Mach numbers.

2.1.3. Omidirectional line-source and point-source solutions

The present analysis first considers the line-source solution, which is then converted to the point-source solution. The modal amplitude of the line source in 2D is given by:

$$A_{(n)} = \frac{1}{\Lambda_{(m,n)}} P_{(n)}(z'), \quad (16)$$

where

$$\Lambda_{(m,n)} = \int_0^H \frac{1}{\rho_j} P_{(n)}(z) P_{(m)}(z) dz. \quad (17)$$

Note that although Eq. (17) is not rigorously orthogonal because of the presence of both the flow and PMLs, it is diagonally dominant, so the modal amplitudes can be approximated by calculating only the diagonals for $\Lambda_{(m,n)}$. This leads to the modal expansion for a line source:

$$p^{\text{line}}(x, z, t) = \frac{i}{2} \sum_{n=1}^N \frac{P_{(n)}(z') P_{(n)}(z) e^{-ik_{r(n)}(x-x'-v_s t)}}{\Lambda_{(n,n)} k_{r(n)}}. \quad (18)$$

When considering the far-field form of a point-source solution, the DSF can be reduced to a series of 2D DSFs corresponding to different azimuths. To account for the $1/R$ spreading of the 2D DSF at each azimuth, the line-source solution is first converted to the point-source solution. Here, $R = \sqrt{(x-x'-v_s t)^2 + (y-y')^2}$ denotes the propagation distance in cylindrical coordinates, where y and y' are the transverse coordinates of the receiver and the moving source, respectively.

Next, the 2D DSF at each azimuth is calculated using the projected Mach number $M_j = v_s \cos \theta / c_j$, where $\theta = \arccos[(x-x'-v_s t)/R]$ is the azimuth angle. This allows us to consider the Doppler shift at field points away from the x - z plane. Note that the projected Mach number is an approximation by neglecting azimuthal coupling described by the derivatives with respect to θ . However, compared to other flow-affected terms, these ones are insignificant in the far field for range-independent problems (Elisseeff and Schmidt, 1997). As demonstrated by Elisseeff and Schmidt (1997), the approximation remains valid for flow velocities up to 100 m/s, albeit with the restriction of a low Mach number. The DSF at each azimuth is given by

$$p^{\text{point}}(x, y, z, t) \approx i\sqrt{2\pi} e^{-\frac{\pi}{4}i} \sum_{n=1}^N \frac{P_{(n)}(z') P_{(n)}(z) e^{-ik_{r(n)}R}}{\Lambda_{(n,n)} \sqrt{k_{r(n)}R}}. \quad (19)$$

It is noteworthy that the eigenvalues and eigenfunctions in the above equation are solved at each azimuth angle θ using the projected Mach number $M_j = v_s \cos \theta / c_j$. This implies that, the depth-separated wave equation, linked to varying Mach numbers $v_s \cos \theta / c_j$ (Eq. (6))) and transformed into the generalized matrix eigenvalue problem (Eqs. (14 to (15))), must be solved multiple times in accordance with different azimuth angles required for the simulation.

2.2. Analytical modal expression for the Doppler-shifted field resulting from a moving directional source

To derive the formula of the DSF generated by a moving directional radiator based on the normal mode theory, it is helpful to start with the free-field, stationary scenario shown in Fig. 3. In the free field, the pressure field produced by a stationary radiator (the directional source) can be considered as an integration of the monopole sources placed on the source surface \mathbf{S} , given by the equation

$$p(x, y, z) = \int_{\mathbf{S}} q(x', y', z') G(x, y, z; x', y', z') dx' dy' dz', \quad (20)$$

where $q(x', y', z')$ represents the strength of the monopole source, and $G(x, y, z; x', y', z')$ is the free-field Green's function given by :

$$G(x, y, z; x', y', z') = \frac{e^{-ik|\mathbf{r}'-\mathbf{r}|}}{|\mathbf{r}'-\mathbf{r}|}, \quad (21)$$

where $\mathbf{r}' = (x', y', z')$ and $\mathbf{r} = (x, y, z)$ denote the position vector of the monopole source and the receiver, respectively.

Applying the Fraunhofer approximation, the far-field form of the product $k|\mathbf{r}'-\mathbf{r}|$ can be approximated as:

$$k|\mathbf{r}'-\mathbf{r}| \approx k|\mathbf{r}_0-\mathbf{r}| - k(\alpha \cos \theta \cos \phi + \beta \sin \theta \cos \phi + \gamma \sin \phi), \quad (22)$$

where $\mathbf{r}_0 = (x_0, y_0, z_0)$ represents the position of the radiator's acoustic center, (θ, ϕ) is the observation angle, and the local coordinate of each monopole source is given by

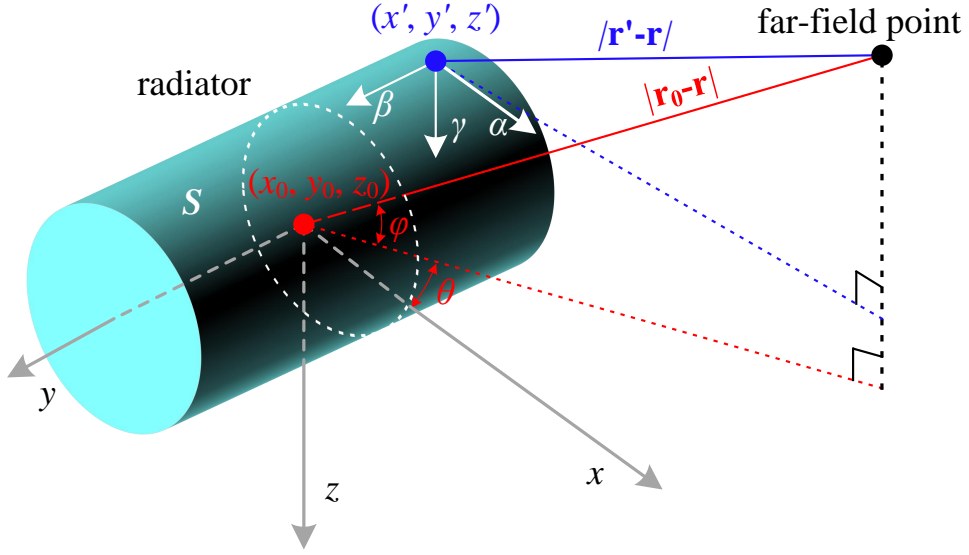


Figure 3: Schematic of the far-field approximation for deriving the directivity of a radiator. The position information is displayed in red and blue for the acoustic center of the radiator and the point placed on the source surface S , respectively.

$$\alpha = x' - x_0, \quad (23a)$$

$$\beta = y' - y_0, \quad (23b)$$

$$\gamma = z' - z_0. \quad (23c)$$

By substituting Eq. (22) back into Eq. (20), the far field of the radiation from the motionless source can be written as

$$p(x, y, z) = \frac{e^{-ik|\mathbf{r}_0 - \mathbf{r}|}}{|\mathbf{r}_0 - \mathbf{r}|} D(\theta, \varphi), \quad (24)$$

where $D(\theta, \varphi)$ is the radiator directivity, which is also known as the scattering function in acoustic scattering problems. $D(\theta, \varphi)$ can be expressed as

$$D(\theta, \varphi) = \int_S q(x_0 + \alpha, y_0 + \beta, z_0 + \gamma) e^{ik(\alpha \cos \theta \cos \varphi + \beta \sin \theta \cos \varphi + \gamma \sin \varphi)} d\alpha d\beta d\gamma, \quad (25)$$

Now, let's consider the same radiator horizontally moving in a shallow water waveguide. The DSF due to the moving radiator can be obtained by replacing the Green's function in Eq. (21) with that determined in the waveguide with uniform flow (Eq. (19)). Substituting Eq. (19) back into Eq. (20) and, after exchanging the order of summation and integration, this yields

$$p(x, y, z, t) = i\sqrt{2\pi}e^{-\frac{\pi}{4}i} \sum_N \frac{P_{(n)}(z)}{\Lambda_{(n,n)}\sqrt{k_{r(n)}}} \int_S q(x', y', z') P_{(n)}(z') \frac{e^{-ik_{r(n)}R}}{\sqrt{R}} dx' dy' dz', \quad (26)$$

Expanding the eigenfunction with the Taylor series at the center depth z_0 and then utilizing the Fraunhofer approximation in the $x - y$ plane, the integration in Eq. (26) can be written as

$$A_{(n)} = \frac{e^{-ik_{r(n)}R_0}}{\sqrt{R_0}} \int_S q(x_0 + \alpha, y_0 + \beta, z_0 + \gamma) \sum_{b=0} \left[\frac{1}{b!} \frac{d^b P_{(n)}(z)}{dz^b} \Big|_{z=z_0} \gamma^b \right] e^{ik_{r(n)}(\alpha \cos \theta + \beta \sin \theta)} d\alpha d\beta d\gamma, \quad (27)$$

where $R_0 = \sqrt{(x - x_0 - v_s t)^2 + (y - y_0)^2}$ represents the horizontal range between the acoustic center and the receiver. The Taylor series can be divided into two parts according to odd and even orders

$$T_{(n)} = T_{o(n)} + T_{e(n)}, \quad (28a)$$

$$T_{o(n)} = \sum_{b=0}^{\infty} \frac{1}{(2b+1)!} \left. \frac{d^{(2b+1)} P_{(n)}(z)}{dz^{2b+1}} \right|_{z=z_0} \gamma^{2b+1}, \quad (28b)$$

$$T_{e(n)} = \sum_{b=0}^{\infty} \frac{1}{(2b)!} \left. \frac{d^{(2b)} P_{(n)}(z)}{dz^{2b}} \right|_{z=z_0} \gamma^{2b}. \quad (28c)$$

The eigenfunctions $P_{(n)}(z)$ satisfy Eq. (3), allowing us to simplify Eq. (28) by reducing the order of derivation of $P_{(n)}(z)$ based on Eq. (3):

$$T_{o(n)} = \left. \frac{dP_{(n)}(z)}{dz} \right|_{z=z_0} \frac{1}{k_{z(n)}} \sin(k_{z(n)}\gamma), \quad (29)$$

$$T_{e(n)} = P_{(n)}(z_0) \cos(k_{z(n)}\gamma), \quad (30)$$

where $k_{z(n)} = \sqrt{\mu^2 k^2 - k_{r(n)}^2}$ is the Doppler-shifted vertical wavenumber

Therefore, Eq. (27) can be rewritten as follows:

$$A_{(n)} = \frac{e^{-ik_{r(n)}R_0}}{\sqrt{R_0}} [A_{o(n)} + A_{e(n)}], \quad (31a)$$

$$A_{o(n)} = \left. \frac{dP_{(n)}(z)}{dz} \right|_{z=z_0} \frac{1}{k_{z(n)}} \int_{\mathbf{S}} q(x_0 + \alpha, y_0 + \beta, z_0 + \gamma) e^{ik_{r(n)}(\alpha \cos \theta + \beta \sin \theta)} \sin(k_{z(n)}\gamma) d\alpha d\beta d\gamma, \quad (31b)$$

$$A_{e(n)} = P_{(n)}(z_0) \int_{\mathbf{S}} q(x_0 + \alpha, y_0 + \beta, z_0 + \gamma) e^{ik_{r(n)}(\alpha \cos \theta + \beta \sin \theta)} \cos(k_{z(n)}\gamma) d\alpha d\beta d\gamma. \quad (31c)$$

By applying the Euler equation to the sine and cosine terms in the above equations, $A_{o(n)}$ and $A_{e(n)}$ can be further rewritten as

$$A_{o(n)} = \frac{1}{2i} \left. \frac{dP_{(n)}(z)}{dz} \right|_{z=z_0} \frac{1}{k_{z(n)}} \int_{\mathbf{S}} q(x_0 + \alpha, y_0 + \beta, z_0 + \gamma) e^{ik_{r(n)}(\alpha \cos \theta + \beta \sin \theta)} [e^{ik_{z(n)}\gamma} - e^{-ik_{z(n)}\gamma}] d\alpha d\beta d\gamma \quad (32)$$

$$A_{e(n)} = \frac{1}{2} P_{(n)}(z_0) \int_{\mathbf{S}} q(x_0 + \alpha, y_0 + \beta, z_0 + \gamma) e^{ik_{r(n)}(\alpha \cos \theta + \beta \sin \theta)} [e^{ik_{z(n)}\gamma} + e^{-ik_{z(n)}\gamma}] d\alpha d\beta d\gamma \quad (33)$$

It should be noted that the Doppler-shifted vertical and horizontal wavenumbers have the following relations

$$k_{r(n)} = k_{(n)} \cos(\varphi_n), \quad (34a)$$

$$k_{z(n)} = k_{(n)} \sin(\varphi_n). \quad (34b)$$

where $k_{(n)} = k + Mk_{r(n)}$ is the Doppler-shifted wavenumber of the n th mode, φ_n is the grazing angle of the up- and down-going plane wave of the n th mode. Using these relations and the formula for directivity given by Eq. (25), Eqs. (32)-(33) can be further reduced to

Table 1

Parameters of shallow-water environment in simulations.

Parameter	Value
Water depth	54 m
Water sound speed	1500 m/s
Water density	1000 kg/m ³
Seabed sound speed	1650 m/s
Seabed sound attenuation	0.0 dB/λ
Seabed density	1900 kg/m ³

$$A_{o(n)} = \frac{1}{2i} \frac{dP_n(z)}{dz} \Big|_{z=z_0} \frac{1}{k_{z(n)}} [D(\theta, \varphi_n, K_n) - D(\theta, -\varphi_n, K_n)] \quad (35)$$

$$A_{e(n)} = \frac{1}{2} P_{(n)}(z_0) [D(\theta, \varphi_n, K_n) + D(\theta, -\varphi_n, K_n)] \quad (36)$$

As a result, the far-field sound pressure generated by the moving radiator in the shallow water waveguide can be obtained by substituting Eq. (31) and Eqs. (35)-(36) back into Eqs. (26)-(27)

$$p(x, y, z, t) = i\sqrt{2\pi}e^{-\frac{\pi}{4}i} \sum_N [A_{o(n)} + A_{e(n)}] P_{(n)}(z) \frac{e^{-ik_{r(n)}R_0}}{\sqrt{k_{r(n)}R_0}}. \quad (37)$$

3. Numerical simulations

In this section, we present the results of numerical simulations. First, we present benchmarking of the proposed theoretical model for underwater acoustic propagation from an omnidirectional moving source. Next, we demonstrate and interpret the Doppler-affected changing modal shapes and eigenvalue shifts using the case of an omnidirectional source. Finally, we consider the case of a moving directional radiator, in which the phenomenon of Doppler beam shift is investigated using the proposed theory. In these simulations, the selection of the basis mode number N followed the same rule as that reported by He et al. (2021). Their suggestion is that computational efficiency and accuracy can be guaranteed by setting $N = 3N_{\text{cut}}$ (where $N_{\text{cut}} = 2Hf/c_1$ represents the number of cut-off basis modes), and this was found to provide a reasonable compromise for the present study; thus, this value was used for the all the simulations conducted in this work. Additionally, in line with the parametric study by He et al. (2021), the PML thickness was set to be 3λ , with $\beta = 5N^{0.25}$. The simulations were implemented using MATLAB (MathWorks, Natick, MA, USA) installed on a laptop with an Intel Core i9-13900K CPU (Intel, Santa Clara, CA, USA) and 128 GB RAM. All simulations considered a point source with unit amplitude, and the sound-field results are given by the level (in decibels) relative to the free-space source level at 1 m. Typically, the free-space source level is of 120 dB *re* $1\mu\text{Pa}^2$ at 1 m in underwater acoustics. This means that, if the pressure observed at a point in the channel is -30 dB, then the actual signal level at the point is 90 dB.

3.1. Moving omnidirectional source

3.1.1. Model validation

We benchmarked the proposed model for the problem of underwater acoustic propagation from a submerged monopole source moving in a two-layer shallow-water waveguide. The benchmark solution was obtained by a 2D wavenumber integration (Schmidt and Kuperman, 1994; Buckingham and Giddens, 2006) that accounts for Doppler effects in 3D. An analytical NM model (Buckingham and Giddens, 2006) was also applied for comparison purposes. The waveguide parameters are given in Table 1. The source was placed at a depth of 6 m and was moving horizontally with a constant velocity of 50 m/s. The source frequency was 84 Hz, below which mode 4 in the water was cut off for a stationary source.

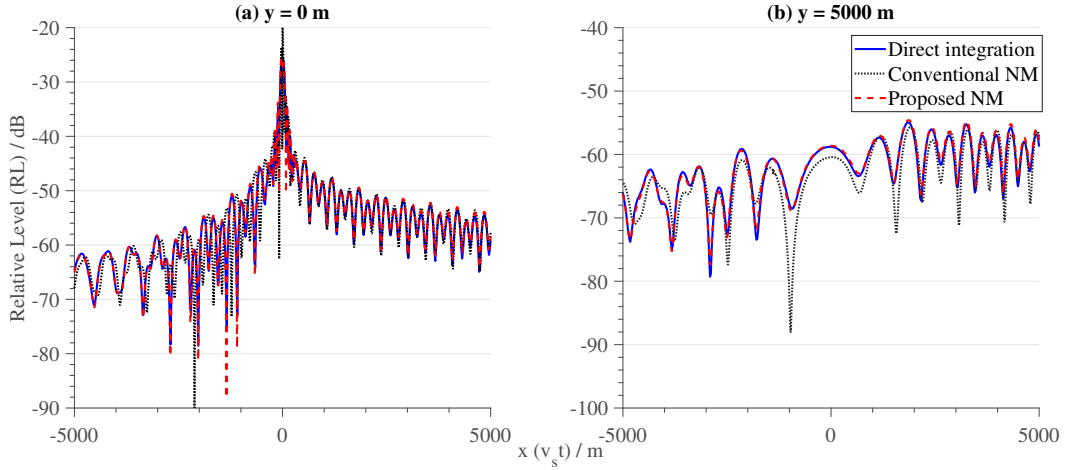


Figure 4: Relative levels (RLs) received at a depth of 30 m in the (a) $y = 0$ m plane and (b) $y = 5000$ m plane from a source moving at a depth of 6 m. The source frequency was 84 Hz. For comparison, the results from 2D wavenumber integration and the conventional NM-based model are shown by the solid blue and dashed-dotted black lines, respectively.

Figure 4 shows plots of the relative levels (RLs) received at 30 m in the $y = 0$ m and $y = 5000$ m planes, where the horizontal axis $v_s t$ represents the horizontal range between the moving source and the point of closest approach to the fixed receiver; the source is approaching the receiver when $v_s t > 0$ m. Figure 4 shows an apparent asymmetric pattern about $v_s t$ due to the Doppler-induced modal cut-offs. The excellent agreement with the wavenumber-integration solution demonstrates the effectiveness of the proposed model in calculating underwater sound propagation from a moving monopole source. As can be seen, there are large discrepancies from the analytical NM model, especially for $v_s t < 0$ m. This demonstrates one advantage of the proposed method over the conventional NM model, i.e., that the contribution of branch-line integrals is accounted for by accommodating higher-order modes. Evanescent modes result from higher-order modes, the attenuating behavior of which coincides with that of the continuous spectrum (branch-line integrals) (He et al., 2021). The analytical NM model considers only the modal contributions and neglects the branch-line integrals that become dominant when a mode is about to be cut off.

Figure 5 shows plots of the RLs in the $y = 0$ m and $z = 35$ m planes, demonstrating visible Doppler-induced modal cut-offs more straightforwardly. These results also confirm the correctness of Eq. (19) in accounting for the Doppler shift at points away from the x - z plane. In Fig 5 (a), a distinct interference transition from three modes to two modes can be observed as the source traverses its closest approach. This phenomenon arises due to the down-shifting of frequency behind the source motion. Specifically, when the source moves outbound relative to the receiver, the frequency decreases from 84 Hz to a value below which mode 3 becomes cut-off. However, the modal cutoff induced by motion does not precisely coincide with the closest approach. The red line annotated in Fig 5 (b) indicates the azimuth angle at which mode 3 initiates its cut-off. A comprehensive discussion and approximation of this angle are provided later in Section 3.1.2.

3.1.2. Effects of the changing modal shape and eigenvalue Doppler shift

To interpret the asymmetric pattern observed in Fig. 5, we present a modal analysis of underwater propagation. This analysis highlights the advantages of our proposed NM model, as it accurately captures the effects of Doppler-induced changes in modal shape and eigenvalue.

Figure 6 presents the first three waterborne modes as functions of θ_1 , which represents the azimuth launch angle between the motion track and the line connecting the source and receiver. The mode shape is determined by extracting the column vector of \mathbf{W} that corresponds to the eigenvalue from the solution to Eq. (15). The first two waterborne mode shapes remain relatively unchanged due to the low Mach number in water. However, the third mode exhibits significant changes in shape, transitioning from a propagating mode to a leaky mode as the source moves from inbound to outbound positions. This behavior corresponds to the modal cut-off observed in Fig. 5. Importantly, it should be noted that such an effect is not accounted for in the conventional NM model, leading to significant discrepancies when compared to the reference solution.

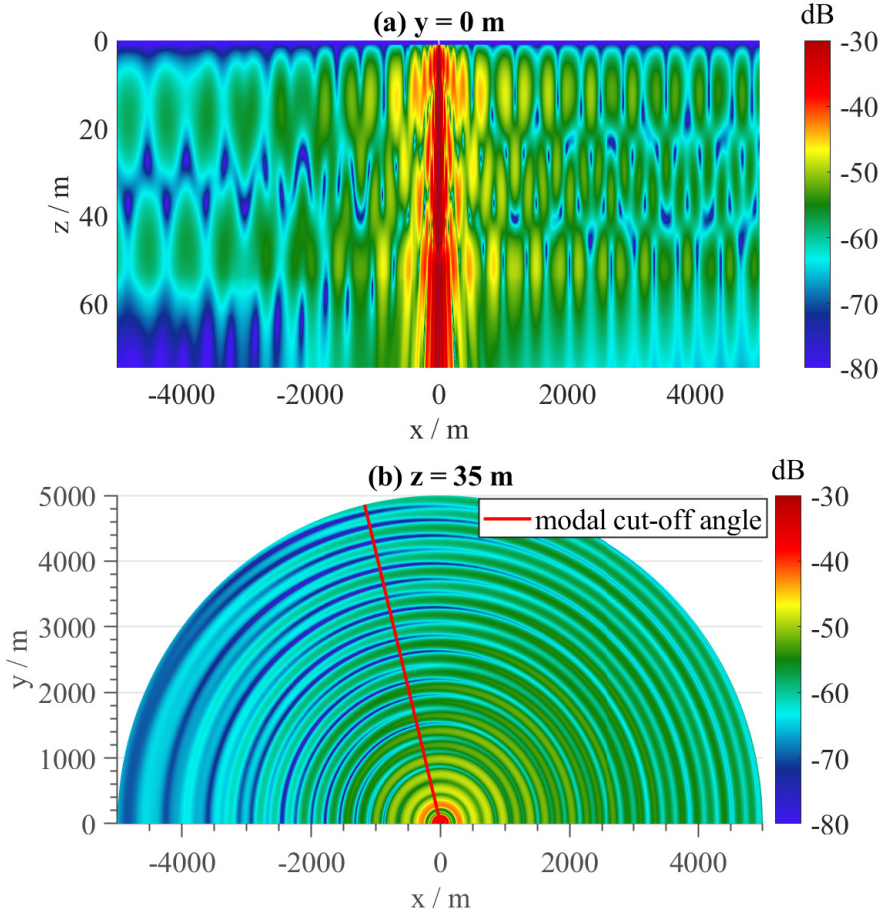


Figure 5: RLs received in the (a) $y = 0$ m plane and (b) $z = 35$ m plane. The source was moving at a depth of 6 m with a source frequency of 84 Hz. The source motion speed was 50 m/s. The red line annotated in the lower row distinguishes the angle where mode 3 starts to cut-off.

Next, we analyze the eigenvalue Doppler shift. To differentiate the Doppler impacts on various modes, it is helpful to express the eigenvalue shift as a frequency shift. Referring to Schmidt and Kuperman (1994), the Doppler-shifted angular frequency for a specific waterborne mode can be expressed as

$$\Omega_{(n)} = \omega + k_{r(n)} v_s \cos \theta_1. \quad (38)$$

Figure 7(a) presents the ratio of the frequency Doppler shift as a function of θ_1 . Due to modal dispersion, different modes exhibit varying Doppler shifts; the lower the mode number, the greater the frequency shift. Consequently, classifying the frequency shifts in the spectrum allows different modes to be distinguished. It is evident that each mode exhibits a pair of lower and upper shifted frequencies, depending on whether the source is moving outbound or inbound relative to the receiver. Specifically, for a given mode, the down-shifted and up-shifted frequencies can be approximated using Eq. (38) by assigning a negative ($\theta_1 > 90^\circ$) or positive ($\theta_1 < 90^\circ$) projected motion speed ($v_s \cos \theta_1$) based on the source-receiver relative position. For the first three modes, the down-shifted and up-shifted frequencies $\left(\frac{\Omega_{(n)}}{2\pi}\right)$ are 81.3 and 86.9 Hz, 81.4 and 86.8 Hz, and 81.6 and 86.6 Hz, respectively. This result confirms that different modes undergo distinct eigenvalue Doppler shifts.

The imaginary part of the eigenvalue corresponding to mode 3, depicted in Fig. 6(b), decreases rapidly and becomes nonzero at around $\theta_1 = 103.5^\circ$. This indicates mode cut-off at a specific azimuth launch angle (θ_c) under the given

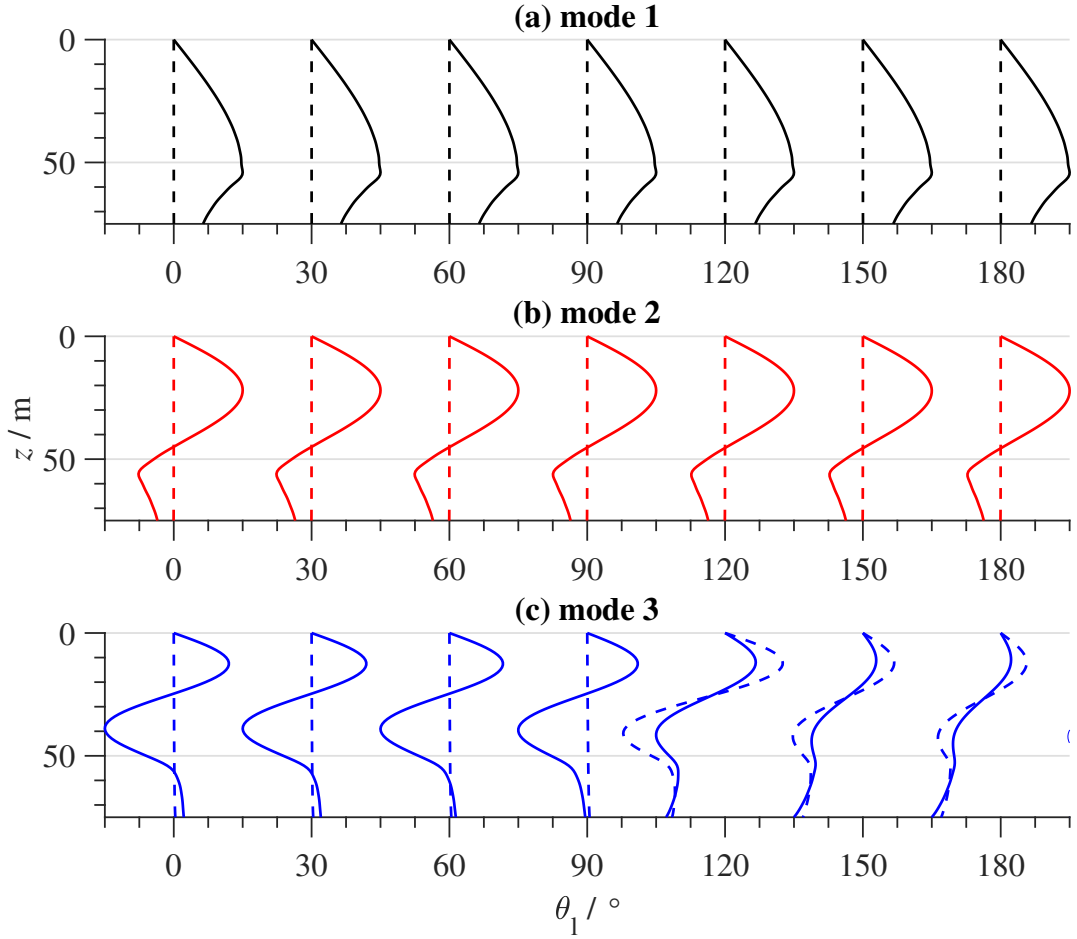


Figure 6: Waterborne mode shape as a function of azimuth launch angle with a source moving from inbound to outbound at a motion speed of 50 m/s at 84 Hz. The solid and dashed lines represent the normalized real and imaginary parts of the mode shapes, respectively. The mode shape is determined by extracting the column vector of \mathbf{W} that corresponds to the eigenvalue from the solution to Eq. (15).

conditions. To estimate θ_c , the Doppler-shifted frequency and the cut-off frequency for mode 3 are presented in the same figure. It is evident that the turning point, where the imaginary part of the eigenvalue starts to drop significantly, aligns with the azimuth launch angle at which the Doppler-shifted frequency approaches the cut-off frequency. Consequently, θ_c can be estimated by equating the frequency Doppler shift $f' = \frac{f}{1 - M \cos \theta_c}$ to the modal cut-off frequency f_c ,

where $f_c = \frac{(n - 0.5)c_1 c_2}{2h \sqrt{c_2^2 - c_1^2}}$. Solving this equation allows one to determine

$$\theta_c = \arccos \left[\frac{1}{M} - \frac{f}{M f_c} \right]. \quad (39)$$

It is essential to acknowledge that Eq. (39) is valid solely for an iso-velocity water column. In the presence of an SSP, this equation may either overestimate or underestimate θ_c , depending on whether the profile exhibits strong down-refraction or up-refraction. Figure 5(b) includes an annotation of θ_c based on Eq. (39), denoting the azimuth launch angle at which the sound field starts to decay as mode 3 transitions into a leaky mode.

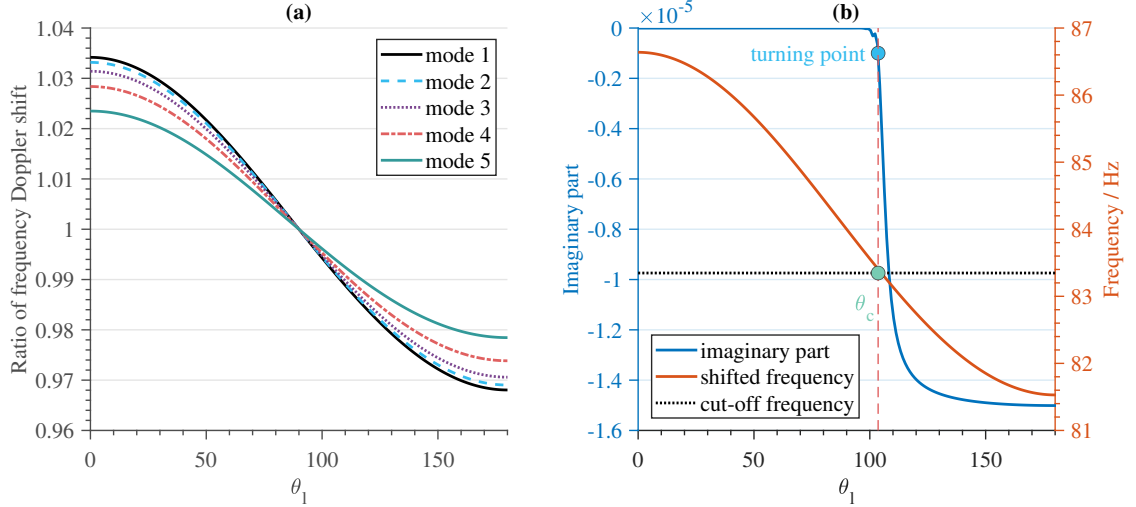


Figure 7: (a) The ratio of the frequency Doppler shift for first five modes as a function of azimuth launch angle θ_1 ; (b) The imaginary part (blue solid line) of the eigenvalue and the frequency Doppler shift (red solid line) for mode 3 as a function of azimuth launch angle θ_1 . The black dashed line annotates the cut-off frequency for mode 3, and the blue and green solid dots represent the turning point, where the eigenvalue for mode 3 starts to become a complex value, and the azimuth angle, at which mode 3 starts to be cut-off, respectively. The source motion speed is 50 m/s, and the unshifted frequency is 84 Hz.

Furthermore, considering the low Mach number in the water, modal cutoff induced by motion may be less pronounced than explored in this article, particularly when the speed of the source motion is extremely low. Specifically, when the sediment is lossy, each mode experiences attenuation as it propagates along the waveguide, the eigenvalue of which transitions from a pure real to a complex number. This mechanism of modal attenuation closely mirrors that observed in the modal cutoff discussed in this article. Consequently, the modal attenuation caused by seabed loss may overshadow that attributed to the source motion, particularly at low speeds. Nonetheless, the motion of the source introduces fore-aft asymmetry into modal attenuation, potentially leading to fore-aft asymmetry in the DSF, especially at lower frequencies (Buckingham and Giddens, 2006).

3.2. Moving directional source

In this section, we present the results of simulations of the DSF excited by a directional source moving in refractive shallow water and examine the phenomenon of Doppler beam shift. In practice, high-spatial-resolution directivity is observed when the source frequency is high. The proposed method enables effective calculations of the DSF by providing a semi-analytical solution. In these simulations, the directional source is defined as a piston-like radiator in the vertical direction and is uniform in the horizontal direction. It is expressed as

$$D(\theta, \varphi, k) = \frac{2J_0(ka \sin(\varphi - \varphi'))}{ka \sin(\varphi - \varphi')}, \quad (40)$$

where a is the radius of the piston-like radiator and φ' is the beam grazing angle. The value of a was set to 1 m, and the initial value of φ' was set to 0° . The environmental parameters of the waveguide remained unchanged from those presented in Table 1, with the exception of the sound speed in the water column. Here, we used the SSP measured during the Shallow Water Experiment 2006 (SWE06)(Tang et al., 2007), as shown in Fig. 8(a), to demonstrate that the derived formula is valid for a refractive shallow-water environment. The source was moving horizontally at $z = 30$ m with a velocity of 100 m/s, and its frequency was set to 5000 Hz.

Figure 8(c) displays the RLs in the $y = 0$ plane for the moving piston-like radiator. For comparison, Fig. 8(b) also shows the case of a moving omnidirectional source. Comparing Figs. 8(b) and 8(c) reveals that the piston-like radiator produces a non-uniform field distribution in the near field and generates a more pronounced focusing effect along the channel axis at $z = 30$ m than the omnidirectional source. Unlike the omnidirectional source, which excites every propagating mode, the piston-like directivity (0° grazing angle) primarily enhances low-order modes that converge

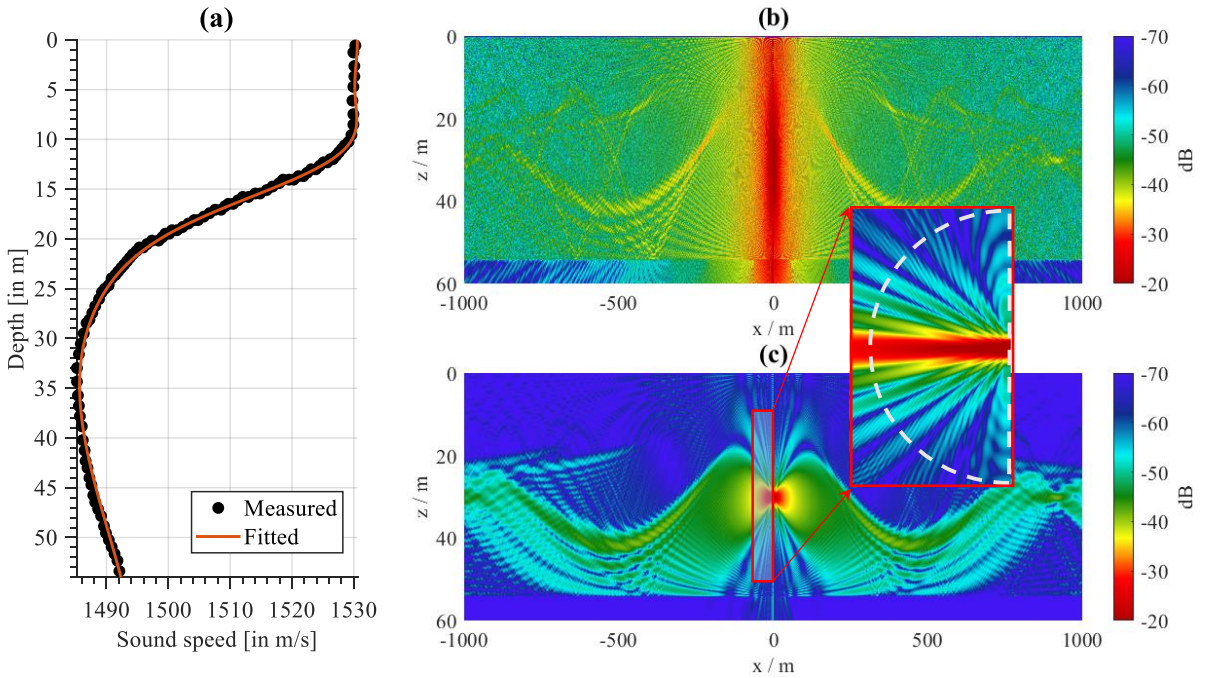


Figure 8: RLs received in the $y = 0$ m plane at 5000 Hz with (b) omnidirectional and (c) directional sources. The SWE06 SSP [shown in panel (a)] is considered in this case, and the source directivity in panel (c) is piston-like. The source motion speed is 100 m/s.

to the channel axis, as indicated by Eq. (37). Consequently, the piston-like radiator scenario exhibits a noticeable channel-axis effect.

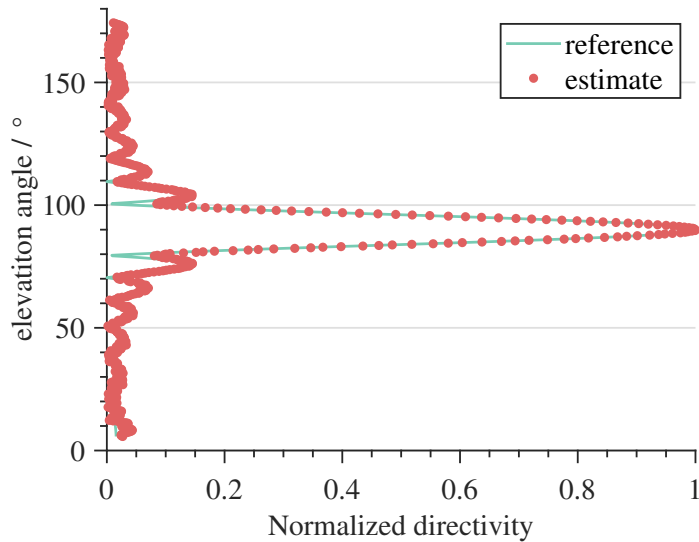


Figure 9: Comparison of the effective directivity evaluated by the near-field DSF on the circle shown in the magnified plot of Fig. 8(c), with the theoretical directivity of a piston-like radiator. The source motion speed is 100 m/s.

Unfortunately, there is currently no benchmark procedure available for verifying the accuracy of the proposed model in the case of a moving directional source. However, to assess the effectiveness of the model, we can consider the effective directivity of the radiator by normalizing the near-field DSF. To do this, we extract the near-field DSF when the source is outbound using a circle with a radius of 20 m, as shown by the dashed white line in the magnified plot of Fig. 8(c). Figure 9 presents the effective directivity evaluated from the near-field DSF, which exhibits excellent agreement with the theoretical directivity. This confirms that the proposed model can reproduce the correct field distribution for a moving directional source.

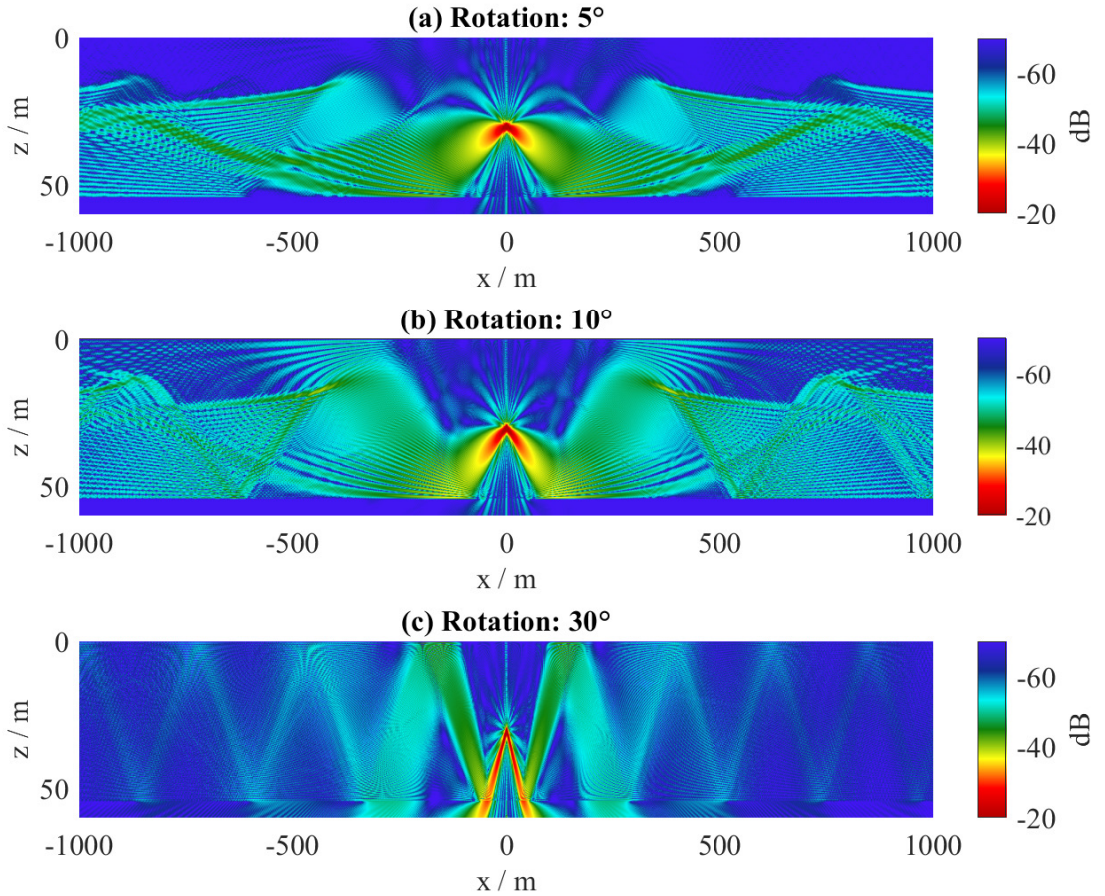


Figure 10: RLs received in the $y = 0$ m plane at 5000 Hz for directional sources with initial beam grazing angles of (a) 5° , (b) 10° , and (c) 30° , respectively. The source motion speed is 100 m/s.

We next investigate the DSFs produced by radiators with varying beam grazing angles φ' , and the corresponding results are shown in Fig. 10. As φ' becomes steeper ($\varphi' = 10^\circ$), the channel-axis propagation gradually diminishes. Instead, the downward-directed beam emitted by the radiator follows a geometry reflection path interacting with the bottom, and this subsequently reappears near the surface to create a zone of high sound intensity, which bends back towards to the seabed before even interacting with the sea surface. When φ' is increased to 30° , surpassing the critical angle of the channel duct (approximately 10°), the beam ray emitted by the radiator escapes from the channel duct, resulting in propagation patterns characterized by surface and bottom bounces without refraction by the SSP. Moreover, since the steep $\varphi' = 30^\circ$ approaches the critical angle of the seafloor (φ_c), the propagation exhibits noticeable attenuation. These results confirm that the proposed model accurately describes the DSFs produced by radiators with different directivities in a refractive shallow-water environment.

3.2.1. Doppler beam shift

Although the DSF pattern shown in Fig. 10 exhibits weak fore–aft asymmetry, as previously observed in Fig. 5, there are considerable differences between the inbound and outbound DSFs. These differences arise from changing modal shapes, eigenvalue shifts, and the shift of the beam emitted by the moving radiator, known as the Doppler beam shift. In this section, we focus on investigating the Doppler beam shift in iso-velocity shallow water using the proposed theory. To specifically analyze the effect of the Doppler beam shift without interference from refraction, we set the water sound speed to a constant value of 1500 m/s, and all other simulation parameters were kept consistent with those used in the simulation corresponding to Fig. 8.

To visualize the Doppler beam shift, Fig. 11 displays the differences in the DSF between the cases of inbound and outbound source motion for three beam grazing angles φ' (by subtracting the DSF when the source moves outbound from that when it moves inbound). The “blue–red” interference pattern of the DSF differences indicates that the beam emitted by the source undergoes a shift when it moves from inbound to outbound. Moreover, steeper grazing angles of the beam are associated with larger beam shifts. According to Eq. (37), the source directionality can be considered as the modal excitation, and the corresponding weighted coefficient is based on the grazing angle of the up- and down-going plane waves of each mode. As the source motion induces the eigenvalue Doppler shift, the grazing angle of the modal plane wave will also shift, resulting in a shift of the modal weighting coefficient compared to the scenario of a stationary source. Therefore, as the source moves from inbound to outbound, the propagating mode excited by the dominant beam energy changes from higher to lower modes, consequently causing the Doppler beam shift.

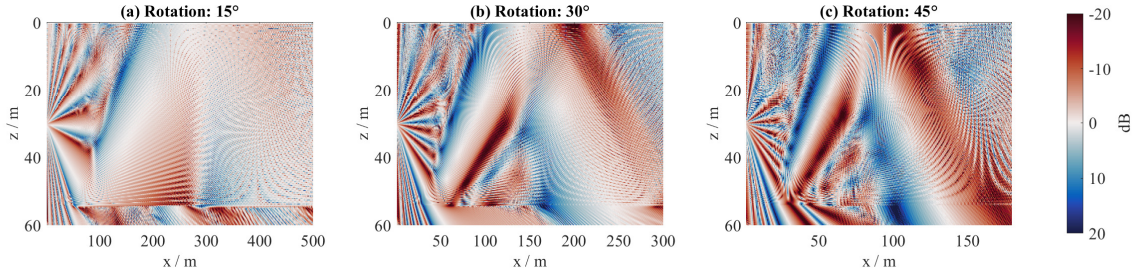


Figure 11: DSF differences between the inbound and outbound cases for beam grazing angles of (a) 15°, (b) 30°, and (c) 45°. The source motion speed is 100 m/s, and the source frequency is 5000 Hz.

To gain insight into the underlying physics of the Doppler beam shift from the perspective of geometric acoustics, we present a ray interpretation that quantitatively links the grazing angles of the beam to the Doppler beam shifts. In Fig. 12, the source \mathbf{S} launches the unshifted beam with a grazing angle of φ' while moving horizontally with velocity v_s . The beam ray ahead of the moving source arrives at the bottom at point A. The beam ray emitted by the same source at rest will arrive at point B ahead of point A. Based on the geometric relation shown in Fig. 12, we can derive the down-shifted beam angle:

$$\Delta\varphi' = \frac{\mathbf{AB} \sin(\varphi')}{\mathbf{SA}} = \frac{v_s \cos \theta_1 \sin(\varphi')}{c_1}. \quad (41)$$

Note that when the source moves outbound, the ray theory assumes that the beam will be up-shifted by the same angular shift as the inbound source motion. Figure 13(a) compares the exact Doppler beam shift with the beam shift approximated by Eq. (41) as functions of φ' . The exact beam shifts are calculated by subtracting the shifted beam for the inbound or outbound source motion from the unshifted beam, with the launch angle set to be 0 and π for the inbound and outbound cases, respectively. The approximated beam shift closely matches the Doppler beam shift but is slightly lower than the inbound Doppler beam shift. This can be explained by the fact that the energy maximum of the beam will be weighted toward the mode represented by a pair of up- and down-going plane waves with a grazing angle of $\pm\varphi'$ relative to the horizontal. When the source is inbound, the grazing angle of each modal plane wave is up-shifted, meaning $\varphi'_{\text{in}} > \varphi'_{\text{out}}$. From the above analysis, it is evident that larger φ' values correspond to larger Doppler beam shifts, which explains the slight discrepancy between the approximated beam shift and the inbound Doppler beam shift as evaluated numerically.

To further validate the proposed theoretical model and its agreement with the ray interpretation, Fig. 13(b) illustrates the Doppler beam shift as a function of the motion speed of the source with a beam grazing angle of 70°.

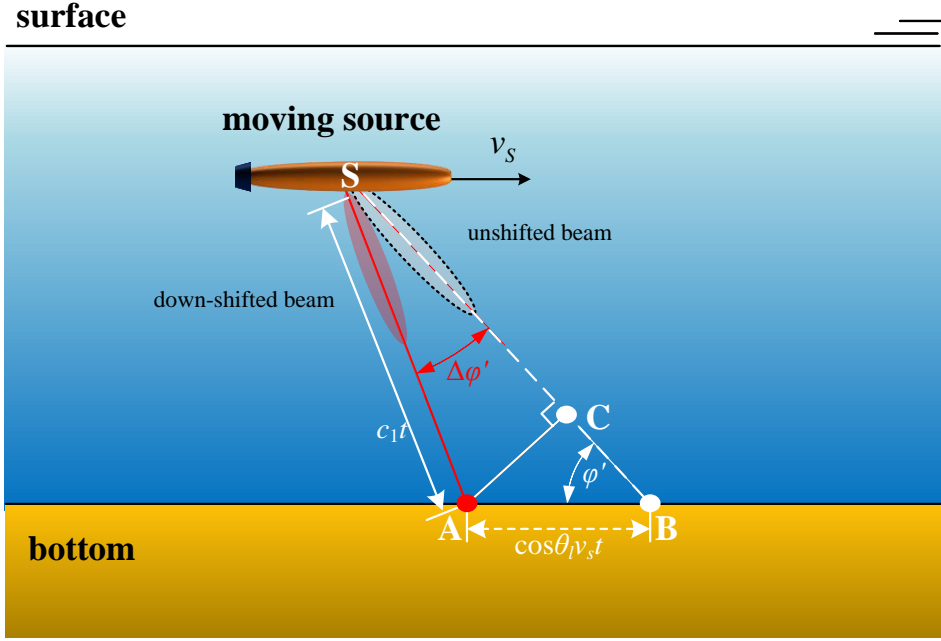


Figure 12: Ray schematic showing the interpretation of the Doppler beam shift.

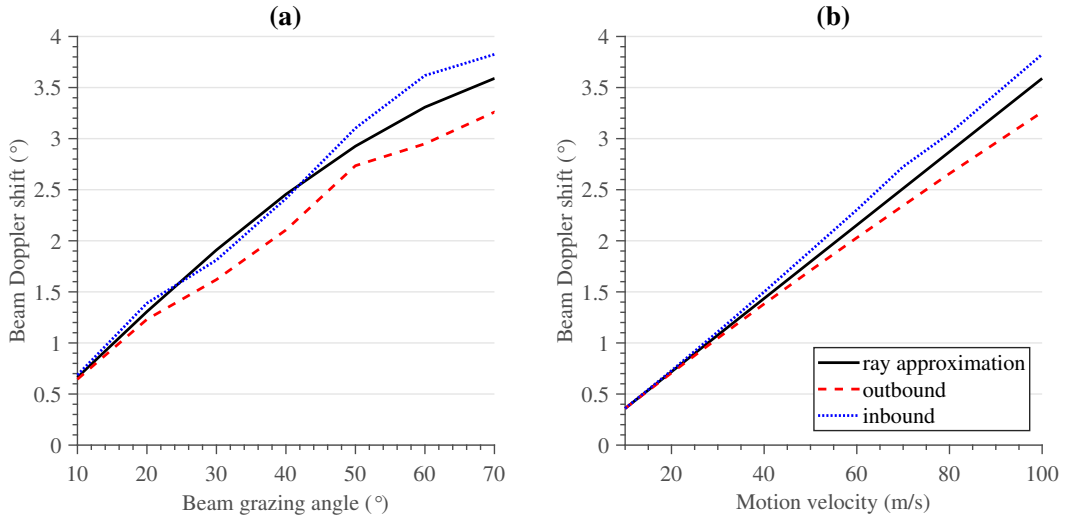


Figure 13: Comparisons of exact Doppler beam shifts evaluated from the proposed model (dotted blue lines and dashed red lines, respectively) with the beam shift approximated by Eq. (41) (solid black lines) as a function of: (a) the beam grazing angle and (b) of the motion speed of the radiator. The source motion speed in (a) is 100 m/s, and the beam grazing angle in (b) is 70° .

Once more, the results obtained from the theoretical model closely align with the predictions from the ray theory, providing further confirmation of the accuracy of Eq. (41) and the overall validity of the theoretical model.

3.2.2. Beam energy transfer

Based on Eq. (41), one might expect that the differences between the inbound and outbound DSFs would monotonically increase with increasing ϕ' . However, it is important to note that the derivation of Eq. (41) assumes a free-field condition, neglecting the waveguide physics. In the presence of the sea surface and seafloor, certain modes

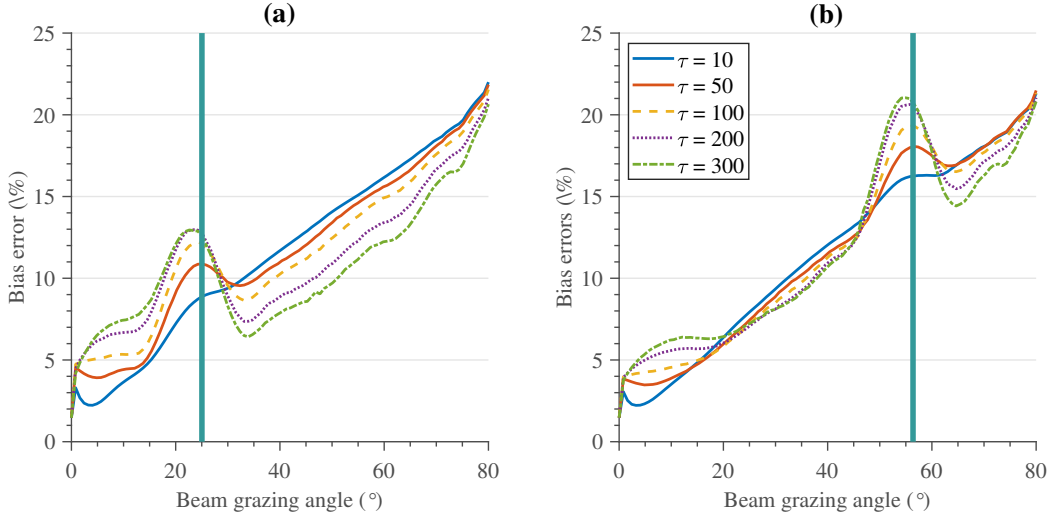


Figure 14: Bias errors (BEs) between the inbound and outbound DSFs for different beam grazing angles for scenarios with (a) a softer seabed with the default parameters and (b) a harder seabed. The dark-cyan vertical lines indicate the critical angle of the seafloor φ_c . The source motion speed is 20 m/s.

are cut off and tend to leak into the seabed half-space based on their modal plane wave's propagating angle, which can be steeper than the critical angle of the seafloor φ_c . Consequently, anomalies in the differences between the inbound and outbound DSFs may occur when the radiator's beam sweeps over φ_c . To demonstrate this, the analysis considers the bias errors (BEs) between the inbound and outbound DSFs for different φ' values. The source motion speed is 20 m/s in this case, and other parameters remain unchanged. The BE is defined

$$\text{BE} = \frac{1}{Q} \sqrt{\frac{\sum_{q=1}^Q (|p_{\text{in}}| - |p_{\text{out}}|)^2}{\sum_{q=1}^Q |p_{\text{in}}|^2}}. \quad (42)$$

For different scenarios of the beam grazing angle φ' . In fairness, the maximum horizontal range used for evaluating BE must cover an equal number of geometric reflections for various beam grazing angles. Thus, the maximum horizontal range is defined as $\tau \frac{h - z'}{\tan(\varphi')}$ for both inbound and outbound source motion, with τ representing a scaling factor controlling the maximum horizontal range. To evaluate the BE, 100 field points were evenly sampled along the vertical direction from $z = 0$ to $z = 54$ m, while the horizontal range was uniformly divided into 1024 samples. The results were obtained in the $y = 0$ m plane. Figure 14 shows the BE as a function of φ' for various horizontal ranges. Additionally, Fig. 14(b) provides a comparison with the case of a hard seafloor, where the density and sound speed are 2200 kg/m³ and 2700 m/s, respectively. The dark-cyan vertical lines in Fig. 14 represent φ_c , which is the critical angle of the seafloor.

The BEs exhibit an overall upward trend with increasing φ' ($< 20^\circ$), and larger errors are observed for larger horizontal ranges. This behavior is attributed to the dominant beam energy exciting propagating modes at shallow φ' , resulting in a phase difference between the inbound and outbound DSFs that accumulates as the horizontal range increases.

For φ' values close to φ_c , pronounced peaks in the BE are observed, with higher peaks corresponding to larger horizontal ranges. This phenomenon occurs because the radiator emits a beam with a certain lobe width, allowing only a fraction of the energy to penetrate the sediment near φ_c . This portion of energy is weighted toward leaky modes, while the remaining energy remains trapped within the waveguide and propagates. As the source moves from inbound to outbound, φ' gradually decreases from above φ_c to below φ_c , leading to a reduction in the total energy of leaky modes. Consequently, the apparent asymmetry in the DSF occurs as φ' sweeps over φ_c .

For φ' values exceeding φ_c , the BE decreases with increasing horizontal range. This can be attributed to the dominant beam energy being weighted toward leaky modes in this scenario. Significant differences between the

inbound and outbound DSFs produced by a moving directional radiator are observed only in short ranges, where leaky modes can temporarily propagate with exponential decay in their amplitudes. The analysis highlights that, apart from changing modal shapes and eigenvalue shifts, the considerable differences between the inbound and outbound DSFs produced by a directional radiator moving in shallow water can be attributed to a third mechanism, known as the Doppler beam shift.

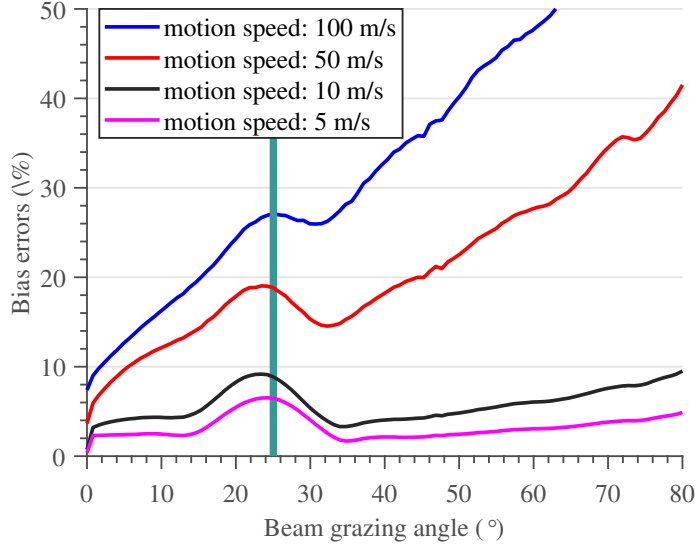


Figure 15: Bias errors (BEs) between the inbound and outbound DSFs as a function of the beam grazing angle for various motion speeds. The dark-cyan vertical lines indicate the critical angle of the seafloor φ_c . The maximum horizontal range is $\tau = 300$. The environment parameters remain the same as those used in Fig 14 (a).

It is crucial to recognize that the Doppler beam shift may be less pronounced than investigated in this article when considering a low-speed source, such as a towed transducer. Nevertheless, the above analysis highlights that the Doppler beam shift depends not only on motion speed but also on the beam grazing angle. Specifically, when beam grazing angle exceeds the seabed critical angle, the fore-aft asymmetry in the DSF resulting from the beam shift remains significant at near propagation ranges. Therefore, a low-speed source with a steep grazing beam may induce detectable fore-aft asymmetry in the DSF at the near-field. Additionally, Figure 15 illustrates the BEs between the inbound and outbound DSFs as a function of the beam grazing angle for different motion speeds. In this case, the maximum horizontal range is set to $\tau = 300$, and other parameters remain default as those used for Fig 14 (a). Despite the fore-aft asymmetry in the DFS weakening as the source slows down, pronounced peaks are still observable at the seabed critical angle, even at a low motion speed of 5 m/s. This suggests that, even for a low-speed directional source, the characteristic of the fore-aft asymmetry in the DFS can be enhanced when the beam grazing angle sweeps the critical angle of the seafloor. This enhancement may prove useful in distinguishing an underwater source operating at a low-speed mode from the same source at rest.

4. Concluding remarks

This paper introduces a semi-analytical method for calculating the DSF resulting from a directional moving source in a range-independent waveguide. The normal-mode model developed here accurately captures Doppler-induced effects, encompassing changes in modal shape, eigenvalue Doppler shift, and branch-line integral contributions. To resolve the eigenproblem of the open waveguide, we implement a PML to truncate the half-space seabed. Subsequently, the eigenmodes of the truncated waveguide are projected onto the space bounded by the sea surface and the outer PML boundary. This projection yields a closed generalized matrix eigenproblem, enabling accurate determination of the eigenvalues. The method ensures that no roots are missed, and it exhibits convergence to an exact solution with increasing numbers of modes, as it explicitly solves the full-wave equation for a homogeneous moving medium.

Additionally, this normal-mode model provides valuable insights into waveguide physics when compared to a fully numerical approach.

Furthermore, based on the principle of wave superposition, we have established an analytical, normal-mode solution for the DSF produced by a moving directional source in the range-independent shallow water. Instead of evaluating the numerical integral of field superposition using an array of equivalent sources, we derive the analytical solution by introducing the Fraunhofer far-field approximation and a Taylor-series expansion to the integral kernel. The analytical solution derived expresses the DSF excited by the moving radiator as a sum over eigenmodes, with the modal excitation determined by the source directivity depending upon the grazing angle of each pair of modal plane waves. The derived modal expression is rigorous and thus valid for any type of directional source moving horizontally in a range-independent environment with an arbitrary SSP.

The proposed theoretical model was employed to investigate the Doppler beam shift produced by a piston-like radiator moving in a two-layer waveguide. The model provided valuable insights, revealing that the Doppler beam shift is due to the angular offset of each pair of modal plane waves. This finding is consistent with the ray theory, and it was observed that steep beam grazing angles lead to significant Doppler beam shifts. Additionally, the analysis demonstrated that the DSF exhibits apparent asymmetry when the beam grazing angle sweeps the critical angle of the seafloor. These results confirm that the Doppler beam shift acts as a new mechanism, causing substantial differences between the fields generated by a moving directional source and by the same source at rest, allowing them to be distinguished. This understanding may find practical applications in underwater acoustic detection of moving targets. The enhanced fore-aft asymmetry in the DSFs, resulting from a moving directional source's beam sweeping over the critical angle of the seafloor, holds potential information for estimating seafloor parameters. This aspect will be further investigated in future work.

Declarations

The authors declare that they have no known competing financial interests or personal relationships that could have appeared to influence the work reported in this paper.

Acknowledgments

This work was supported by the National Natural Science Foundation of China (Grant No. 12304499 and Grant No. 52271343), and the Stable Supporting Fund of National Key Laboratory of Underwater Acoustic Technology (Grant No. JCKYS2023604SSJS018). The authors would like to thank the two anonymous reviewers, whose helpful comments and suggestions have greatly improved the manuscript.

References

- Amiri-Simkooei, A., Snellen, M., Simons, D.G., Buckingham, M., 2008. Estimating the frequency dependent behavior of marine sediment sound speeds using low frequency aircraft sound. *The Journal of the Acoustical Society of America* 123, 3349–3349.
- Barsikow, B., King, W., 1988. On removing the doppler frequency shift from array measurements of railway noise. *Journal of Sound Vibration* 120, 190–196.
- Berenger, J.P., 1994. A perfectly matched layer for the absorption of electromagnetic waves. *Journal of computational physics* 114, 185–200.
- Bevans, D.A., Buckingham, M.J., 2017. Estimating the sound speed of a shallow-water marine sediment from the head wave excited by a low-flying helicopter. *The Journal of the Acoustical Society of America* 142, 2273–2287.
- Buckingham, M.J., Giddens, E.M., 2006. Theory of sound propagation from a moving source in a three-layer Pekeris waveguide. *The Journal of the Acoustical Society of America* 120, 1825–1841.
- Buckingham, M.J., Giddens, E.M., Simonet, F., Hahn, T.R., 2002. Propeller noise from a light aircraft for low-frequency measurements of the speed of sound in a marine sediment. *Journal of Computational Acoustics* 10, 445–464.
- Clark, J., Flanagan, R., Weinberg, N., 1976. Multipath acoustic propagation with a moving source in a bounded deep ocean channel. *The Journal of the Acoustical Society of America* 60, 1274–1284.
- Dzieciuch, M., Munk, W., 1994. Differential doppler as a diagnostic. *The Journal of the Acoustical Society of America* 96, 2414–2424.
- Elisseeff, P., Schmidt, H., 1997. Acoustic propagation through a low mach number, stratified flow. *The Journal of the Acoustical Society of America* 101, 1936–1944.
- Flanagan, R., Weinberg, N.L., Clark, J., 1974. Coherent analysis of ray propagation with moving source and fixed receiver. *The Journal of the Acoustical Society of America* 56, 1673–1680.
- Fu, Z., Xi, Q., Li, Y., Huang, H., Rabczuk, T., 2020. Hybrid fem–sbm solver for structural vibration induced underwater acoustic radiation in shallow marine environment. *Computer Methods in Applied Mechanics and Engineering* 369, 113236.

- Guthrie, A., Fitzgerald, R., Nutile, D., Shaffer, J., 1974. Long-range low-frequency cw propagation in the deep ocean: Antigua-newfoundland. *The Journal of the Acoustical Society of America* 56, 58–69.
- Haijie, S., Jinghua, L., Lili, L., Yidan, S., 2019. Flight parameters measurement based on underwater acoustic signal processing, in: 2019 IEEE 2nd International Conference on Information Communication and Signal Processing (ICICSP), IEEE. pp. 290–294.
- Hawker, K.E., 1979. A normal mode theory of acoustic doppler effects in the oceanic waveguide. *The Journal of the Acoustical Society of America* 65, 675–681.
- He, T., Humphrey, V.F., Mo, S., Fang, E., 2020. Three-dimensional sound scattering from transversely symmetric surface waves in deep and shallow water using the equivalent source method. *The Journal of the Acoustical Society of America* 148, 73–84.
- He, T., Mo, S., Guo, W., Fang, E., 2021. Modeling propagation in shallow water with the range-dependent sea surfaces and fluid seabeds using the equivalent source method. *The Journal of the Acoustical Society of America* 149, 997–1011.
- He, T., Wang, B., Mo, S., Fang, E., 2023a. Predicting range-dependent underwater sound propagation from structural sources in shallow water using coupled finite element/equivalent source computations. *Ocean Engineering* 272, 113904.
- He, T., Wang, B., Tang, S., Zhou, F., Mo, S., Fang, E., 2023b. Numerical simulation of wave propagation in ice-covered ocean environments based on the equivalent-source method. *Physics of Fluids* 35.
- Jensen, F.B., Kuperman, W.A., Porter, M.B., Schmidt, H., 2011. *Computational ocean acoustics*. Springer Science & Business Media.
- Jiang, L.W., Zou, M.S., Liu, S.X., Huang, H., 2020. Calculation method of acoustic radiation for floating bodies in shallow sea considering complex ocean acoustic environments. *Journal of Sound and Vibration* 476, 115330.
- Lo, K.W., Ferguson, B.G., 2013. Flight parameter estimation using instantaneous frequency measurements from a wide aperture hydrophone array. *IEEE Journal of Oceanic Engineering* 39, 607–619.
- Lowson, M., 1965. The sound field for singularities in motion. *Proceedings of the Royal Society of London. Series A. Mathematical and Physical Sciences* 286, 559–572.
- Makarewicz, R., 1992. Influence of doppler and convection effects on noise propagation. *Journal of sound and vibration* 155, 353–364.
- Neubert, J.A., 1977. The effect of doppler on long-range sound propagation. *The Journal of the Acoustical Society of America* 62, 1404–1411.
- Nijs, L., Wapenaar, C., 1990. The influence of wind and temperature gradients on sound propagation, calculated with the two-way wave equation. *The Journal of the Acoustical Society of America* 87, 1987–1998.
- Obrezanova, O.A., Rabinovich, V.S., 1998. Acoustic field generated by moving sources in stratified waveguides. *Wave Motion* 27, 155–167.
- Ostashev, V.E., Wilson, D.K., 2015. *Acoustics in moving inhomogeneous media*. CRC Press.
- Petris, G., Cianferra, M., Armenio, V., 2022. A numerical method for the solution of the three-dimensional acoustic wave equation in a marine environment considering complex sources. *Ocean Engineering* 256, 111459.
- Pierce, A.D., Beyer, R.T., 1990. *Acoustics: An introduction to its physical principles and applications*. 1989 edition.
- Rabinovich, D., Givoli, D., Bécache, E., 2010. Comparison of high-order absorbing boundary conditions and perfectly matched layers in the frequency domain. *International Journal for Numerical Methods in Biomedical Engineering* 26, 1351–1369.
- Rabinovich, V., Hernández Juárez, J., 2016. Effective methods of estimates of acoustic fields in the ocean generated by moving sources. *Applicable Analysis* 95, 124–137.
- Schmidt, H., Kuperman, W.A., 1994. Spectral and modal representations of the doppler-shifted field in ocean waveguides. *The Journal of the Acoustical Society of America* 96, 386–395.
- Shen, C., Cai, G., He, Z., Huang, W., Zhu, Z., 2016. A parameterized doppler distorted matching model for periodic fault identification in locomotive bearing. *Proceedings of the Institution of Mechanical Engineers, Part C: Journal of Mechanical Engineering Science* 230, 3791–3802.
- Singer, I., Turkel, E., 2004. A perfectly matched layer for the helmholtz equation in a semi-infinite strip. *Journal of Computational Physics* 201, 439–465.
- Stoker, R., Guo, Y., Street, C., Burnside, N., 2003. Airframe noise source locations of a 777 aircraft in flight and comparisons with past model-scale tests, in: 9th AIAA/CEAS Aeroacoustics Conference and Exhibit, p. 3232.
- Tang, D., Moum, J.N., Lynch, J.F., Abbot, P., Chapman, R., Dahl, P.H., Duda, T.F., Gawarkiewicz, G., Glenn, S., Goff, J.A., et al., 2007. Shallow water’06: A joint acoustic propagation/nonlinear internal wave physics experiment. *Oceanography* 20, 156–167.
- Vecherin, S.N., Keith Wilson, D., Ostashev, V.E., 2011. Incorporating source directionality into outdoor sound propagation calculations. *The Journal of the Acoustical Society of America* 130, 3608–3622.
- Vecherin, S.N., Wilson, D.K., Ostashev, V.E., 2012. Application of the equivalent source method to directional noise sources. *Noise Control Engineering Journal* 60, 137–147.
- Waldvogel, J., 2006. Fast construction of the fejer and clenshaw–curtis quadrature rules. *BIT Numerical Mathematics* 46, 195–202.
- Zhang, H., Zhang, S., He, Q., Kong, F., 2016. The doppler effect based acoustic source separation for a wayside train bearing monitoring system. *Journal of Sound and Vibration* 361, 307–329.
- Zhong, J., Zou, H., Lu, J., 2023. A modal expansion method for simulating reverberant sound fields generated by a directional source in a rectangular enclosure. *The Journal of the Acoustical Society of America* 154, 203–216.